

Landau–Ginzburg–Devonshire Theory for the Temperature–Grain Size Phase Diagram of BaTiO₃ Nanoceramics

K.-O. JANG^a, I.-H. KIM^{a,*}, K.-H. HO^a,
I.-H. KIM^a, C.-J. KIM^b AND U.-B. RI^a

^a*Faculty of Physics, Kim Hyong Jik University of Education, Ryul-dong 100, Tongdaewon District, Pyongyang, Democratic People's Republic of Korea*

^b*Faculty of Chemistry, Kim Il Sung University, Ryongnam-dong 98, Taesong District, Pyongyang, Democratic People's Republic of Korea*

Received: 24.10.2024 & Accepted: 19.05.2025

Doi: [10.12693/APhysPolA.147.463](https://doi.org/10.12693/APhysPolA.147.463)

*e-mail: dawei_0660@163.com

The temperature and grain size dependences of the ferroelectric phase transitions and dielectric properties of BaTiO₃ nanoceramics are described by higher-order Landau–Ginzburg–Devonshire theory. A structurally stable 8th-order Landau–Ginzburg–Devonshire potential with the 2nd- and 4th-order coefficients varying with temperature and grain size is proposed for a phenomenology of BaTiO₃ nanoceramics. The temperature–grain size phase diagram constructed on the basis of this potential model describes well the experimentally observed cubic–tetragonal–orthorhombic and cubic–orthorhombic–rhombohedral triple points and ferroelectric to paraelectric to ferroelectric reentrance phenomenon. The spontaneous polarization and dielectric constant of BaTiO₃ nanoceramics are calculated. It is shown that dielectric anomalies appear at the phase transitions and dielectric peaks are depressed, and diffused with decreasing grain size.

topics: BaTiO₃ nanoceramics, Landau–Ginzburg–Devonshire potential, structural stability, grain size effect

1. Introduction

BaTiO₃ (BT) is one of the most widely used ferroelectric materials, even almost 80 years after its discovery, since it is an environmentally friendly ferroelectric and has excellent dielectric, electromechanical, and optical properties. Recently, with the rapid development of modern microelectronics, the size effects in BaTiO₃ nanomaterials such as thin films, nanowires, nanotubes, nanoparticles, and nanoceramics have attracted great interest of researchers [1–5]. As the clarification of ferroelectric properties in BaTiO₃ nanoceramics is related to the improvement of the performance of multilayer ceramic capacitors (MLCCs), thermistors, electrooptic devices, etc. [6–8], the influence of grain size, temperature, and pressure on their structure and physical properties has been studied actively both experimentally and theoretically.

Zhao et al. [9] systematically investigated the phase transitions and susceptibility of BaTiO₃ ceramics with grain sizes in the range of 50–1200 nm. The experimental results showed a decrease in the Curie–Weiss temperature with decreasing grain size, and the critical size corresponding to the

suppression of ferroelectricity was estimated to be 10–30 nm at room temperature. Buscaglia et al. [10], Pithan et al. [11], Deng et al. [12], and Buscaglia et al. [13] confirmed that the nanocrystalline ceramics with average grain sizes of 50, 35, 30, and 20 nm exhibit tetragonal ferroelectricity, and the cubic (C)–tetragonal (T) phase transition temperature (the Curie temperature) depends on the grain size. However, there is some experimental evidence supporting the existence of the orthorhombic (O) phase at room temperature. Frey et al. [14] showed the absence of tetragonal lattice distortions and the existence of the orthorhombic structure in BaTiO₃ ceramics with grain sizes below 100 nm at room temperature. In [15–20], it was reported that the reduction of the grain size leads to enhanced stability of the O phase. Polotai et al. [19] proposed a generalized temperature–grain size phase diagram of BaTiO₃ nanoceramics based on the experimental data [19–24]. On the other hand, there are experimental data on the ferroelectric–paraelectric–ferroelectric reentrance phenomenon, indicating that ferroelectricity appears again with a further decrease in grain size. Zhu et al. [25] measured the dielectric constant and Curie temperature under hydrostatic pressure and observed

the reentrance phenomenon from the paraelectric C phase to the ferroelectric rhombohedral (R) one with the reduction of grain size to 15 nm. Li et al. [26] reported that paraelectric–ferroelectric phase transition temperatures of BaTiO₃ nanoceramics and nanoparticles with sizes of 2.5–100 nm increase obviously with decreasing grain size.

The Landau phenomenological theory provides a reliable description of a system’s equilibrium behavior near a phase transition [27]. As the results obtained from the theory are determined by the symmetry of the system, it is very useful to analyze the phase transitions using it. Thus, the phenomenological Landau–Ginzburg–Devonshire (LGD) theory of the phase transition is widely used to explain the symmetry changes in nanoscale materials as well as bulk ones [3, 4, 9, 25, 28–37]. Recently, great advances in describing and predicting the phase transitions and the ferroelectric properties of BaTiO₃ nanoceramics have been made using the LGD theory. Buessem et al. [29] explained the increase in average dielectric permittivity in fine-grained BaTiO₃ ceramics below the grain size of a few micrometers by using modified Devonshire’s free energy function in terms of strain and polarization first. Zhao et al. [9] and Ricinchi et al. [30] explained the size effect on the ferroelectric properties and the C–T phase transition of BaTiO₃ ceramics by the Landau–Devonshire theory based on a 6th-order expansion in terms of polarization p . Fang et al. [31, 32] considered the surface effect of BaTiO₃ nanoceramics using the LGD theory based on a 6th-order expansion in terms of polarization components p_i ($i = 1, 2, 3$), assuming that the 2nd-order coefficient depends on temperature and grain size and the 4th-order one on grain size. Fang et al. [33] proposed an 8th-order potential model, assuming that the 2nd-order coefficient depends on temperature, grain size, and radius of the shell, while the other coefficients are constant. Recently, the higher-order LGD theory based on the 8th-order potential model [34] used to describe the nonlinearity of the physical properties of bulk BaTiO₃ has been applied effectively to the phenomenological study on BaTiO₃ nanoceramics [25, 35–37]. The 8th-order potential model is written as

$$\begin{aligned} \Phi(p_i) = & \alpha_1(T) (p_1^2 + p_2^2 + p_3^2) + \alpha_{11} (p_1^4 + p_2^4 + p_3^4) \\ & + \alpha_{12} (p_1^2 p_2^2 + p_2^2 p_3^2 + p_1^2 p_3^2) + \alpha_{111} (p_1^6 + p_2^6 + p_3^6) \\ & + \alpha_{112} [p_1^2(p_3^4 + p_2^4) + p_2^2(p_1^4 + p_3^4) + p_3^2(p_1^4 + p_2^4)] \\ & + \alpha_{123} p_1^2 p_2^2 p_3^2 + \alpha_{1111} (p_1^8 + p_2^8 + p_3^8) \\ & + \alpha_{1112} [p_1^6(p_2^2 + p_3^2) + p_2^6(p_1^2 + p_3^2) + p_3^6(p_1^2 + p_2^2)] \\ & + \alpha_{1122} (p_1^4 p_2^4 + p_2^4 p_3^4 + p_1^4 p_3^4) \\ & + \alpha_{1123} (p_1^4 p_2^2 p_3^2 + p_2^4 p_1^2 p_3^2 + p_3^4 p_1^2 p_2^2), \end{aligned} \quad (1)$$

where $\alpha_1(T)$ is a temperature-dependent coefficient, and the other coefficients are constant.

Lin et al. [35] studied the grain size effect on the phase transitions and dielectric properties of BaTiO₃ nanoceramics by using the modified 8th-order potential model in which the coefficients of (1), i.e., $\alpha_1(T)$ and α_{12} , were written as the function of grain size $\alpha_1^*(T, d)$ and $\alpha_{12}^*(d)$. The theoretical phase diagram predicted the ferroelectric reentrance phenomenon and explained well the changes in the C–T, T–O, and O–R transition temperatures, but two triple points (C–T–R and T–O–R) were remarkably different from those in the experimental phase diagram [19]. Sun et al. [36] estimated the size effect on the ferroelectric phase transitions in BaTiO₃ nanoceramics by using the LGD theory based on the 8th-order potential model in which the compressive stress was inversely proportional to the square of grain size and the shear stress to the grain size. Zhu et al. [25] investigated the phase transitions in BaTiO₃ nanoceramics by using the 8th-order LGD potential with varying coefficients $\alpha_{12}^*(d)$ and $\alpha_1^*(T, \sigma, d)$ to take into account the interaction between internal compressive stresses and hydrostatic pressure and internal shear stresses. They explained quantitatively the experimentally observed ferroelectric reentrance phenomenon.

However, most high-order potential models used in phenomenological studies of BaTiO₃ nanoceramics were constructed through a semi-empirical perturbation approach.

Existing phenomenological theories of BaTiO₃ nanoceramics have not been able to explain the qualitative characteristics of experimental phase diagrams, including the two triple points (C–T–O and C–O–R) in the generalized phase diagram [19] and the stabilization of the O phase observed with decreasing grain size at room temperature [14, 16, 19]. This requires a new phenomenology by which the qualitative characteristics of the ferroelectric properties and the phase transitions observed experimentally in barium titanate (BT) nanoceramics can be accurately described.

According to the singularity theory [38–42], it is impossible to build the structurally stable Landau potential model describing qualitatively the properties of the thermodynamical system using the perturbation approach. Structurally unstable potential models in phenomenology yield incorrect results. Here, the term “structurally stable potential” refers to the potential that yields qualitatively the same results if a small perturbation is added to the potential.

Recently, the methods of construction of the structurally stable LGD potential model have been investigated using the singularity theory and Poincaré normal form theory [41–47]. They have been applied to various materials [41–53]. However, in the phenomenological studies on the phase transitions in BaTiO₃ nanoceramics, the structural stability of the LGD potential has not been considered, so the existing experimental data have not been correctly explained.

The purpose of this work is to propose a structurally stable thermodynamical potential model that allows us to describe the characteristics of phase transitions, such as triple points and ferroelectric reentrance phenomenon, as well as dielectric properties in BaTiO₃ nanoceramics.

2. Structurally stable LGD potential

The structurally stable LGD potential model should be chosen in order to describe all the qualitative characteristics of the phase transitions, because the physical phenomena in crystals are closely related to phase transitions.

The experimental studies such as X-ray diffraction, Raman scattering, and dielectric and specific heat measurements of BaTiO₃ nanoceramics confirm that they undergo the phase transition sequence $Pm3m$ – $P4mm$ – $Bmm2$ – $R3m$ from paraelectric phase $Pm3m$ upon varying temperature, pressure, and grain size [19–26].

The group theoretical analysis shows that the LGD potential describing these phase transitions is expanded as a power series of 3 basis invariants of the image group $m3m$, which are composed of polarization components p_i ($i = 1, 2, 3$). The basis invariants of the image group $m3m$ are as follows [43]

$$\begin{aligned} J_1 &= p_1^2 + p_2^2 + p_3^2, \\ J_2 &= p_1^2 p_2^2 + p_2^2 p_3^2 + p_3^2 p_1^2, \\ J_3 &= p_1^2 p_2^2 p_3^2. \end{aligned} \quad (2)$$

The LGD potential is written as follows

$$\begin{aligned} \Phi &= \Phi_0 + a_1 J_1 + a_2 J_2 + a_{11} J_1^2 + a_3 J_3 + a_{12} J_1 J_2 \\ &+ a_{111} J_1^3 + a_{1111} J_1^4 + a_{1112} J_1^2 J_2 + a_{113} J_1 J_3 \\ &+ a_{22} J_2^2 + a_{11111} J_1^5 + a_{11112} J_1^3 J_2 + a_{1113} J_1^2 J_3 \\ &+ a_{1122} J_1 J_2^2 + a_{23} J_2 J_3 + a_{111111} J_1^6 + a_{222} J_2^3 \\ &+ a_{33} J_3^2 + a_{111112} J_1^4 J_2 + a_{11113} J_1^3 J_3 + \dots \end{aligned} \quad (3)$$

The polynomials constituting the potential Φ form a ring $R[J]$. According to singularity theory, the structurally stable Landau thermodynamical potentials $\Phi[J(\eta)]$ coincide with the degree of accuracy of “small perturbation” near the critical point (the term “critical point” refers to the point where $\partial\Phi[J(\eta)]/\partial\eta = 0$ holds). The perturbation is written as [40–43]

$$I_{\nabla\Phi} = \sum_{k,l=1}^q \chi_k(J) (\nabla J_k, \nabla J_l) \frac{\partial\Phi(J)}{\partial J_l}. \quad (4)$$

On the other hand, if we apply the Poincaré transformation $P = p + \partial H[J(p)]/\partial p$ as the near-identity changes of coordinates, the small perturbation written as (4) is expressed as

$$\frac{\partial H}{\partial J_k} (\nabla J_k, \nabla J_l) \frac{\partial\Phi_0}{\partial J_l}. \quad (5)$$

Hence, the terms expressed by (5) can be considered in the potential (3) as a perturbation [44, 46, 47]. These terms represent the elements of the gradient ideal $I_{\nabla\Phi}$ obtained by applying to the potential (3) the vector field

$$U_k = (\nabla J_k, \nabla J_l) \frac{\partial}{\partial J_l}. \quad (6)$$

The singularities of all the potentials with differences in the elements of $I_{\nabla\Phi}$ are the same because they result in the state equation with the same solutions. That is, they describe the same critical points, phase diagrams, and anomalies of susceptibilities. Therefore, the structurally stable potential model is determined by the local algebra $Q = R[J]/I_{\nabla\Phi}$ as the quotient ring of the polynomial ring $R[J]$ by the ideal $I_{\nabla\Phi}$.

Given the basis invariants, the order and form of the structurally stable potential are determined by the expansion coefficient parameters varying with external parameters such as temperature, pressure, etc. In [50], the structurally stable thermodynamical potential models invariant under the cubic point group $m3m$ were calculated for sets of various varying parameters.

Among the various models [50], we have to choose the model by which we can adequately explain the characteristics of the phase transitions in BaTiO₃ nanoceramics. This is possible by constructing a phase diagram in the space of the varying parameters of the phenomenological model (the coefficient phase diagram), because the generic topological features of the experimental phase diagram, such as the configuration of each phase, the critical points, etc., are reflected in the coefficient phase diagram. The number and order of critical points are determined by varying parameters, while the form of the coefficient phase diagram is determined by the expansion coefficient (constant coefficient or moduli) independent of the external parameters [41]. In [50], the coefficient phase diagrams in the spaces of the various varying parameters were calculated, and the possible coefficient phase diagrams in (a_1, a_2, a_{11}) and (a_1, a_2, a_3) spaces were presented. These results can be used efficiently to choose of the phenomenological model for BaTiO₃ nanoceramics.

The experimental studies on BaTiO₃ nanoceramics were carried out with varying temperature, grain size, and pressure. According to the singularity theory, the number of varying parameters in the LGD potential should not be less than the number of external parameters (experimental parameters) [54]. Comparing the experimental data for the temperature–grain size phase diagram of BaTiO₃ nanoceramics with the coefficient phase diagrams [50], it can be concluded that the coefficient phase diagram a_1 – a_2 of the 8th-order potential model with the varying parameters a_1 , a_2 , and a_{11} can explain the experimental data for tricritical point (C–T–O and C–O–R) and C–R reentrance phenomenon. Thus, it is possible to explain

TABLE I

Structurally stable potential models with varying parameters a_1 , a_2 , and a_{11} invariant under the cubic point group $m\bar{3}m$ [50].

Structurally stable potentials $\Phi(J)$	The highest order
$\Phi_1 = a_1 J_1 + a_2 J_2 + a_{11} J_1^2 + a_3 J_3 + a_{12} J_1 J_2 + a_{111} J_1^3 + a_{112} J_1^2 J_2 + a_{22} J_2^2$	8
$\Phi_2 = a_1 J_1 + a_2 J_2 + a_{11} J_1^2 + a_3 J_3 + a_{12} J_1 J_2 + a_{111} J_1^3 + a_{13} J_1 J_3 + a_{22} J_2^2$	8
$\Phi_3 = a_1 J_1 + a_2 J_2 + a_{11} J_1^2 + a_3 J_3 + a_{12} J_1 J_2 + a_{111} J_1^3 + a_{13} J_1 J_3 + a_{112} J_1^2 J_2$	8
$\Phi_4 = a_1 J_1 + a_2 J_2 + a_{11} J_1^2 + a_3 J_3 + a_{12} J_1 J_2 + a_{111} J_1^3 + a_{13} J_1 J_3 + a_{1111} J_1^4$	8
$\Phi_5 = a_1 J_1 + a_2 J_2 + a_{11} J_1^2 + a_3 J_3 + a_{12} J_1 J_2 + a_{111} J_1^3 + a_{112} J_1^2 J_2 + a_{1111} J_1^4$	8

the phase transitions in the BaTiO₃ nanoceramics using the potential model with varying parameters a_1 , a_2 , and a_{11} .

The possible structurally stable potentials with varying parameters a_1 , a_2 , and a_{11} are listed in Table I.

The five potential models in Table I are the family of functions with the same singularity. The thermodynamical potential models Φ_1 – Φ_5 yield the phase diagrams with the same critical points and topological configuration.

By calculating the coefficient phase diagrams of the potential models Φ_1 – Φ_5 , we can find out that the characteristics of the phase diagram of BaTiO₃ nanoceramics can be described adequately by the coefficient phase diagram of the following potential

$$\begin{aligned} \Phi = & a_1(T, d)J_1 + a_2(T, d)J_2 + a_{11}(T, d)J_1^2 + a_3 J_3 \\ & + a_{12} J_1 J_2 + a_{111} J_1^3 + a_{112} J_1^2 J_2 + a_{22} J_2^2 \\ & + a_{1111} J_1^4. \end{aligned} \quad (7)$$

We have investigated the phase diagrams in the space of the varying parameters (a_1 , a_2 , a_{11}) of the potential (7) and shown some of them in Fig. 1a-d. All the features can be seen from the two-dimensional cross-sections in the a_1 – a_2 plane. The phase diagrams reproducing the sequence of the first-order phase transitions C–T–O–R, the triple points (C–T–O and C–O–R), and the ferroelectric reentrance phenomenon are interesting for describing the experimental data of phase transitions for BaTiO₃ nanoceramics. Therefore, only the coefficient phase diagrams with such characteristics are shown in Fig. 1. Each figure panel corresponding to the different ranges of the constant coefficients (moduli) shows the different forms of the phase diagram. The coefficient phase diagrams can adequately reproduce the qualitative characteristics of the experimental temperature–grain size phase diagram. Thus, it has been concluded that the LGD potential model (7) with the varying parameters a_1 , a_2 , and a_{11} can become the phenomenological model for the ferroelectric phase transitions in BaTiO₃ nanoceramics.

3. Temperature–grain size phase diagram

The dependence of the potential (7) on thermodynamic variables is determined by the varying parameters a_1 , a_{11} , and a_2 . Thus, we have first studied the dependence of these parameters on the external thermodynamic variables. Since the volume fraction of the surface becomes significant in nanoceramic grains, strong surface effects can arise. It was found experimentally that the surface tension effect can be assimilated to the application of hydrostatic pressure P [55]. It has been reported that in fine-grained BaTiO₃ with grain size (~ 300 – 500 nm), there are no 90° twins, which strongly reduces the internal stress in the coarse ceramics, and that the single domain is energetically favorable [9, 15]. Thus, the resulting stresses can no longer be relieved by the twinning process.

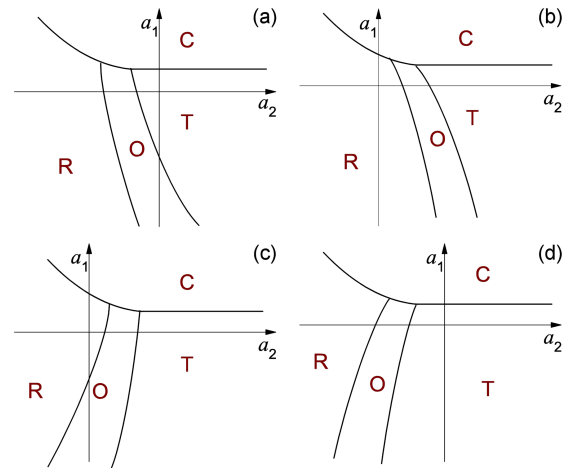


Fig. 1. Section a_1 – a_2 of the coefficient phase diagram a_1 – a_2 – a_{11} of the potential (7). (a) $a_{11} < 0$, $a_{12} > 0$, $a_{112} < 0$, $a_{22} < 0$, (b) $a_{11} < 0$, $a_{12} < 0$, $a_{112} < 0$, $a_{22} < 0$, (c) $a_{11} < 0$, $a_{12} < 0$, $a_{112} > 0$, $a_{22} < 0$, and (d) $a_{11} < 0$, $a_{12} > 0$, $a_{112} > 0$, $a_{22} < 0$. Solid lines represent the first-order phase transition lines between neighboring phases.

TABLE II

Coefficient parameters of (7); T is the temperature given in °C.

Coeff.	Values	Units
a_1	$(T - 113) \times 3.7665 \times 10^5 + \frac{K_1}{(d - d_0)}$	$\frac{\text{V} \cdot \text{m}}{\text{C}}$
a_{11}	$(3.6378 T - 2338.8) \times 10^5 + \frac{K_{11}}{(d - d_0)}$	$\frac{\text{V} \cdot \text{m}^5}{\text{C}^3}$
a_2	$(1.6296 T - 6.963.2) \times 10^5 + \frac{K_2}{(d - d_0)}$	$\frac{\text{V} \cdot \text{m}^5}{\text{C}^3}$
a_{111}	9.1098×10^8	$\frac{\text{V} \cdot \text{m}^9}{\text{C}^5}$
a_{12}	-1.2112×10^9	$\frac{\text{V} \cdot \text{m}^9}{\text{C}^5}$
a_3	1.8568×10^{10}	$\frac{\text{V} \cdot \text{m}^9}{\text{C}^5}$
a_{1111}	4.1311×10^{10}	$\frac{\text{V} \cdot \text{m}^{13}}{\text{C}^7}$
a_{112}	-4.4134×10^{10}	$\frac{\text{V} \cdot \text{m}^{13}}{\text{C}^7}$
a_{22}	-6.6692×10^{10}	$\frac{\text{V} \cdot \text{m}^{13}}{\text{C}^7}$
K_1	0.335	$\frac{\text{V} \cdot \text{m}^2}{\text{C}}$
K_{11}	1	$\frac{\text{V} \cdot \text{m}^6}{\text{C}^3}$
K_2	-7.75	$\frac{\text{V} \cdot \text{m}^6}{\text{C}^3}$
d_0	13.4×10^9	m

On the other hand, since the individual crystallites are surrounded by grain boundaries in ceramics, the compressive stress caused by the elastic three-dimensional clamping of the crystallite may affect the structure and properties of the materials. The shear stress cannot be ignored. The experiments showed that the contribution of the shear stress may increase with decreasing grain size. Consequently, such grain size effect on the physical properties of the nanoceramics should be taken into account in the LGD potential. It was observed experimentally that the hydrostatic pressure and variation of the Curie temperature T_C can be written as d^{-1} and $-d^{-1}$, respectively, where d is the diameter of the grain [55]. Considering the above experimental data [25, 31, 35, 37], the 2nd- and 4th-order coefficients of the LGD potential are assumed to be inversely proportional to the grain size of the ceramics. Generalizing those relations to the varying coefficients $a_1(T, d)$, $a_{11}(T, d)$, and $a_2(T, d)$ of (7), renormalized coefficients can be assumed as follows

$$\begin{cases} a_1 = a_1^0(T - T_0) + \frac{K_1}{d - d_0} \\ a_2 = a_2^0 T + a_2^1 + \frac{K_2}{d - d_0} \\ a_{11} = a_{11}^0 T + a_{11}^1 + \frac{K_{11}}{d - d_0} \end{cases}, \quad (8)$$

where T_0 is the Curie–Weiss temperature, which is equal to 113°C for BaTiO. Analyzing the coefficient phase diagrams (Fig. 1), we can see that the experimental temperature–grain size phase diagram can

TABLE III

Experimental data used for the determination of the coefficient parameters [56–58].

	Experimental values	Values used for calculations
Transition temperatures [°C]		
T_{C-T}	123 [56]	123
T_{T-O}	5 [56]	10
T_{O-R}	-90 [56]	-80
T_0	113 [56]	113
Dielectric constants and piezoelectric constants [pC N ⁻¹]		
ϵ^c	10000 [56]	15000 at 123°C
d_{33}^t	107 [57]	88 at 25°C
ϵ_{11}^t	5000 [56]	4400 at 25°C
ϵ_{33}^o	100 [56]	134 at -60°C
ϵ_{22}^o	3000 [56]	3580 at -60°C
Polarizations [pC cm ⁻²]		
p_s^t	0.18 [56]	0.18 at 123°C
p_s^t	0.26 [56]	0.26 at 25°C
p_s^o	~ 0.2 [56]	0.2045 at 10°C
p_s^o	~ 0.25 [56]	0.2254 at -60°C
Electrostrictive coefficients [m ² C ⁻¹]		
Q_{11}	0.10 [58]	0.10
Q_{12}	-0.034 [58]	-0.034
Q_{44}	0.029 [58]	0.029

be adequately explained on the basis of the figure panel (a). Therefore, the ranges of the constant coefficients of the model (7) are as follows

$$a_3 > 0, \quad a_{111} > 0, \quad a_{12} > 0, \quad a_{112} < 0, \quad a_{22} < 0. \quad (9)$$

The values of the constant coefficient parameters of (7) can be determined from experimental data, taking into account the above relation. Considering the experimental data for the spontaneous polarization, dielectric constant, and piezoelectric constant [56–58], we have calculated constant coefficient parameters (Table II). Experimental data used for the determination of the constant coefficients are shown in Table III, where T_{C-T} , T_{T-O} , and T_{O-R} represent the C–T, T–O, and O–R phase transition points, respectively. In (8), $d_0 = 13.4 \times 10^{-9}$ m has been selected in order to fit quantitatively the experimentally observed T_C for the 15 nm BaTiO₃ ceramic sample [25].

The effect of temperature and grain size on the phase transitions in BaTiO₃ nanoceramics can be seen in the temperature–grain size phase diagram. Using Table II and (7), we have obtained 3 polar phases (lower symmetry phases): (i) the T phase with $p_1 = p_2 = 0, p_3 = p_t \neq 0$; (ii) the O phase with $p_2 = 0, p_1 = p_3 = p_o \neq 0$; (iii) the R phase with

$p_1 = p_2 = p_3 = p_r \neq 0$. The phase transition line between coexisting phases is determined from the equality of their potentials and the state equations. The potentials for each phase are as follows

$$\Phi_C = 0, \quad (10)$$

$$\Phi_T = a_1 p_t^2 + a_{11} p_t^4 + a_{111} p_t^6 + a_{1111} p_t^8, \quad (11)$$

$$\Phi_O = 2a_1 p_o^2 + (4a_{11} + a_2) p_o^4 + (8a_{111} + 2a_{12}) p_o^6 + (16a_{1111} + 4a_{112} + a_{22}) p_o^8, \quad (12)$$

$$\Phi_R = 3a_1 p_r^2 + 3(3a_{11} + a_2) p_r^4 + (27a_{111} + 9a_{12} + a_3) p_r^6 + 9(9a_{1111} + 3a_{112} + a_{22}) p_r^8. \quad (13)$$

The C–T phase transition line is determined from the equality of the potentials of the C and T phases and the state equation of the T phase,

$$\begin{cases} \Phi_C = \Phi_T, \\ \frac{\partial \Phi_T}{\partial p_t} = a_1 + 2a_{11} p_t^2 + 3a_{111} p_t^4 + 4a_{1111} p_t^6 = 0. \end{cases} \quad (14)$$

The C–T phase transition line is determined based on the following equations

$$T = \frac{a_{11}^1 K_1 + a_1^0 K_{11} T_0 + 2K_1 a_{111} p_t^2 + (3K_1 a_{1111} + K_{11} a_{111}) p_t^4 + 2K_{11} a_{1111} p_t^6}{a_1^0 K_{11} - a_{11}^0 K_1},$$

$$d = d_0 + \frac{a_{11}^0 K_1 - a_1^0 K_{11}}{(a_{11}^1 + a_1^0 T_0) a_1^0 + 2a_1^0 a_{111} p_t^2 + (3a_1^0 a_{1111} + a_{11}^0 a_{111}) p_t^4 + 2a_{11}^0 a_{1111} p_t^6}. \quad (15)$$

Similarly, the other phase transition lines are obtained.

The theoretical temperature–grain size phase diagram is shown in Fig. 2. In order to detail the phase diagram in the range from a few nm to several tens of nm, it is presented on a logarithmic scale for grain size. Experimental data [19–25] are also shown for comparison. This phase diagram shows that the phase transition temperatures T_{T-O} and T_{O-R} increase with decreasing grain size, while T_{C-T} decreases. It also indicates the first-order phase transition sequence R–O–T–C occurring with increasing temperature. At room temperature ($T = 25^\circ\text{C}$), the stabilization of the O phase is enhanced with decreasing grain size, and the O phase appears below 100 nm. It is also seen that ferroelectricity disappears with decreasing grain size, and the phase transition from the paraelectric C phase to the ferroelectric R one is induced with further decreasing grain size. There are also C–T–O and C–O–R triple points.

The calculation results are in good agreement with the data of X-ray diffraction [9, 19, 20, 23], dielectric [21, 22] and specific heat [24] measurements for BaTiO₃ nanoceramics. For comparison, the experimental data are shown in Fig. 3 together with the calculated data.

The physical properties of crystals are closely related to the symmetry of the structure. Therefore, from the theoretical phase diagram, it can be seen that the symmetry changes and the physical phenomena observed in BaTiO₃ nanoceramics with varying temperature and grain size can be adequately explained on the basis of the thermodynamic potential model (7).

4. Polarization and dielectric properties

4.1. Temperature and grain size dependences of spontaneous polarization

When varying the external thermodynamic variables such as temperature and grain size, BaTiO₃ nanoceramics undergo phase transitions from the paraelectric C phase to the ferroelectric (T, O, and R) ones, which are accompanied by the occurrence of spontaneous polarization.

The spontaneous polarization in each phase is determined by the state equation $\partial\Phi/\partial p_i = 0$ ($i = 1, 2, 3$). Considering (11), p_t — the spontaneous polarization of the T phase — is determined as follows

$$p_t = \frac{\sqrt{-3a_{111}\Delta^{1/3} + \Delta^{2/3} - 24a_{11}a_{1111} + 9a_{111}^2}}{2\sqrt{3a_{1111}\Delta^{1/3}}}, \quad (16)$$

where

$$\begin{aligned} \Delta &= 108a_{1111}(a_{11}a_{111} - 2a_1a_{1111}) - 27a_{111}^3 + a_{1111} \\ &\times \left[123 \left(a_{11}^2 (32a_{1111}a_{11} - 9a_{111}^2) - 108a_1a_{1111} \right) \right. \\ &\left. \times (a_{11}a_{111} + a_1a_{1111}) + 27a_1a_{111}^3 \right]^{1/2}. \end{aligned} \quad (17)$$

The spontaneous polarizations of the O and R phases are determined similarly.

The spontaneous polarizations of the T, O, and R phases, i.e., p_t , p_o , and p_r , depend on temperature and grain size through the varying coefficient parameters a_1 , a_2 , and a_{11} , respectively. The dependence of the polarization on temperature at the grain sizes of 25, 50, and 100 nm is shown in Fig. 3.

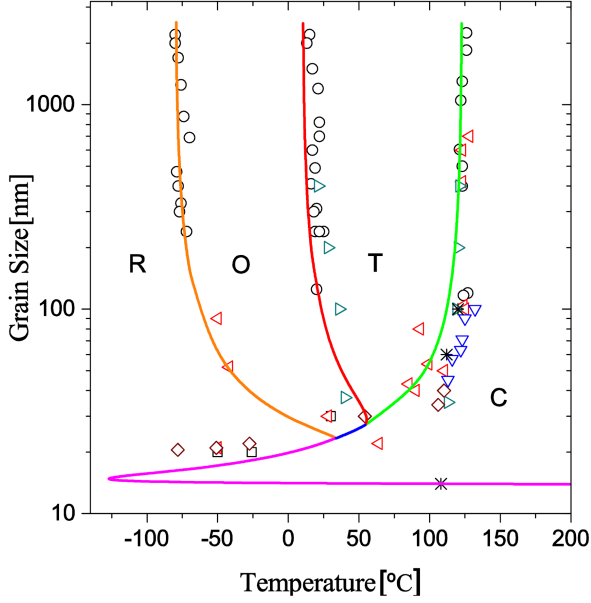


Fig. 2. Theoretical temperature–grain size phase diagram. The experimental data points marked with symbols are taken from the references (○ from [19], □ from [20], ◁ from [21], ▷ from [22], ◇ from [23], ▽ from [24], * from [25]). The phase transition lines calculated in this work are shown with the colored lines (green — C–T line, red — T–O line, orange — O–R line, pink — C–R line, blue — C–O line).

With decreasing temperature, the spontaneous polarizations increase and experience discontinuous jumps at the transition points.

4.2. Dielectric property

Using the potential model (7) and data from Table II, we have studied the change in dielectric property in BaTiO₃ nanoceramics. There are grain boundary layers with a lower dielectric constant due to the surface effect in the grains of nanoceramics [22, 59]. Taking into account the grain boundary effect, the total dielectric constant ε is written as follows [33, 35]

$$\varepsilon = \frac{3\varepsilon_d(\varepsilon_g + 2\varepsilon_d)}{\varepsilon_g + 2\varepsilon_d - (\varepsilon_g - \varepsilon_d)\left(\frac{d}{d+2l}\right)} - 2\varepsilon_d, \quad (18)$$

where ε_d and l are the low dielectric constant in the grain boundary layer and its effective thickness, respectively, and ε_g is the average dielectric constant which is determined by the average dielectric susceptibility $\bar{\chi}$ as follows

$$\varepsilon_g = \bar{\chi} + 1, \quad (19)$$

$$\bar{\chi} = \frac{1}{3}(\chi'_{11} + \chi'_{22} + \chi'_{33}). \quad (20)$$

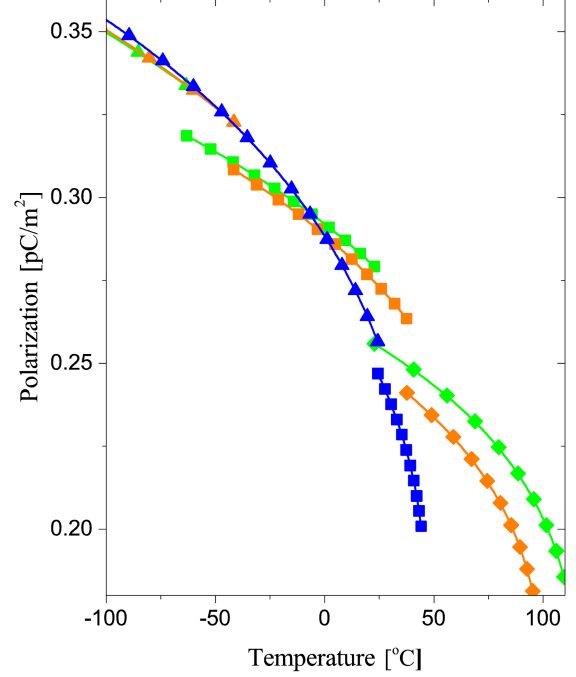


Fig. 3. Temperature dependence of the polarization at the various grain sizes. The grain sizes are identified by color (green — 100 nm, orange — 50 nm, blue — 25 nm). The symbols correspond to the values of polarization in the T phase (◆), O phase (■), and R phase (▲).

Equation (20) is attributed to the fact that the dielectric susceptibility of ceramics is isotropic. Here, χ'_{ij} ($i, j = 1, 2, 3$) are the components of the dielectric susceptibility tensor in the new coordinate system, in which the direction c' is parallel to the polarization direction (see the Appendix for details).

The total dielectric constant of BaTiO₃ nanoceramics has been calculated using the effective thickness $l = 1.98$ nm and low dielectric constant $\varepsilon_d = 90$ [32]. The temperature dependences of the total dielectric constants are shown in Fig. 4 as solid lines for the grain sizes of 25, 50, 90, and 100 nm. It can be seen that there are three dielectric jumps at the grain sizes of 50, 90, and 100 nm, which represent three phase transitions of the R–O, O–T, and T–C. Figure 4 shows that the jump values of the total dielectric constants decrease, and the dielectric peaks become clearly more diffused, lowered, and rounded with decreasing grain size. For example, the dielectric jumps at the C–T phase transition are $\Delta\varepsilon_{100} \approx 2200$ and $\Delta\varepsilon_{50} \approx 70$ at the grain sizes of 100 and 50 nm, respectively. The dielectric peaks move to higher temperatures at the O–R and T–O transition points, while to lower temperatures at the C–T points with decreasing grain size. These results agree with the experimental data [9, 16, 26]. For comparison, the experimental data and the results of the previous phenomenology are shown. The results of dielectric constant

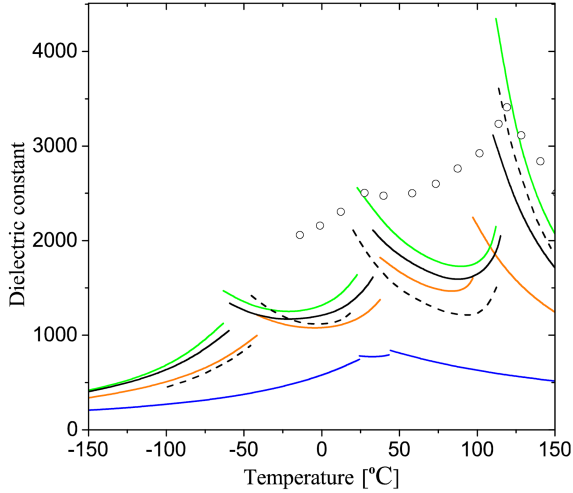


Fig. 4. Temperature dependence of the total dielectric constant at various grain sizes. Grain sizes are identified by color (green — 100 nm, black — 90 nm, orange — 50 nm, blue — 25 nm). Open symbols indicate the experimental data [14], and dashed lines — the previously calculated ones [35].

measurements of BaTiO₃ ceramics with 90 nm grain size are indicated by the symbol “O”. The experimental data show the dielectric anomalies corresponding to C–T and T–O phase transitions around 113°C and –25°C, respectively. Our theoretical results correctly explain such phase transition characteristics. The fact that the dielectric peak decreases with decreasing temperature also explains the experimental data well. These features are consistent with the dielectric measurements of [9].

However, the calculated data show a relatively lower value than the experimental ones. This is due to the assumption of the single domain state, the grain boundary effect, and the size effect of the grains in ceramics, which are taken into account in the potential, while the contribution of these effects decreases with increasing particle size. The dashed lines in Fig. 4 show the calculation results of [35]. As shown in the figure, our calculation results are closer to the experimental data of [14] than the calculation data of [35].

The grain size dependences of the total dielectric constants at the temperatures of –50, 25, and 80°C are shown in Fig. 5. It can be seen from this figure that the total dielectric constant decreases with decreasing temperature and jumps at transition points. It is predicted that the dielectric constants are very small in the R phase (in the grain size range of 12–17 nm).

In Fig. 6, the calculation results for the dielectric constant at room temperature are compared with the experimental data [9, 13, 15, 16, 60]. In the figure, the calculated results of the grain size dependence of the dielectric constant at room temperature are shown with solid lines, and the

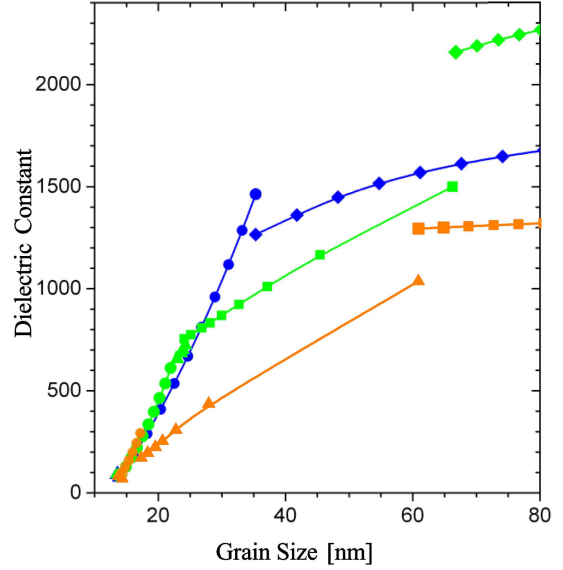


Fig. 5. Grain size dependence of the total dielectric constant at the fixed temperatures. The temperatures are identified by color (blue — 80°C, green — 30°C, orange — –50°C). Symbols hold the same meanings as in Fig. 4.

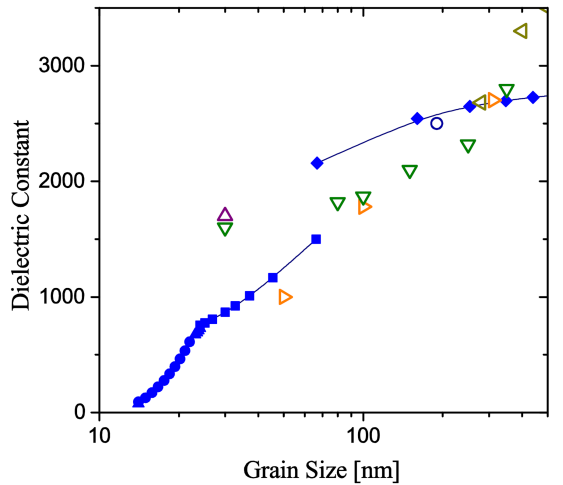


Fig. 6. Grain size dependence of the total dielectric constant at room temperature (25°C). Solid symbols hold the same meanings as in Fig. 4. Open symbols indicate data taken from experimental data (▷ — Zhao et al. [9], △ — Buscaglia et al. [13], ◁ — Arlt [15], ○ — Li [16], and ▽ — Wang et al. [60]).

experimental data are shown with symbols. The calculated results show that there is a dielectric jump at the grain sizes of 14, 23, and 67 nm at room temperature, and the dielectric constant increases with increasing grain size.

Meanwhile, it can be seen that the dielectric measurement data increase rapidly in the $d > 100$ nm range, but the theoretical data increase slower than the experimental ones. This discrepancy is related

to the consideration of the effect of the boundary layer with lower values of dielectric constant on the total dielectric constant, as shown in (18). As the grain size increases, the fraction of the boundary layer in the total volume decreases, resulting in a decrease in the effect of the boundary layer. Hence, the calculated results can be expected to increase slightly compared to the experimental data for larger grain sizes.

5. Discussion

BaTiO₃ nanoceramics with the perovskite structure experience the first-order phase transitions from the C phase to the T, O, and R phases with varying temperature and grain size. According to the results of the group theory, the LGD potential describing these phase transitions is expanded as a power series in 3 basis invariants (2) of the image group $m3m$, which are composed of the ferroelectric polarization components. When applying the higher-order LGD potential to study the phase transition, due to the difficulty of its direct application in practice, simplified structurally stable potential models should be used. Simplification and reduction of the higher-order LGD potential without changing its singularity have been studied previously in [41–49]. In recent studies [46, 50–53], the various structurally stable LGD potentials invariant under the cubic point group $m3m$ have been found.

To consider the structural stability of the previous potential models used in the phenomenological studies of BaTiO₃ nanoceramics, let us express them in terms of the basis invariants (see (2)). The 6th-order potential model [31, 32] and the 8th-order one [25, 35–37] are respectively expanded as follows [50]

$$\begin{aligned} \Phi(J) = & a_1 J_1 + a_{11} J_1^2 + a_2 J_2 + a_{111} J_1^3 + a_{12} J_1 J_2 \\ & + a_3 J_3, \end{aligned} \quad (21)$$

$$\begin{aligned} \Phi(J) = & a_1 J_1 + a_{11} J_1^2 + a_2 J_2 + a_{111} J_1^3 + a_{12} J_1 J_2 \\ & + a_3 J_3 + a_{1111} J_1^4 + a_{112} J_1^2 J_2 + a_{22} J_2^2 \\ & + a_{13} J_1 J_3, \end{aligned} \quad (22)$$

where $a_1 = \alpha_1$, $a_{11} = \alpha_{11}$, $a_2 = \alpha_{12}$, $a_{111} = \alpha_{111}$, $a_{12} = \alpha_{112}$, ...

According to the singularity theory, the singularity of the potential model is determined by its expansion coefficients varying with external parameters such as temperature, pressure, grain size, etc. One (a_1) or two (a_1 and a_2) coefficients in (21) and (22) were assumed to be dependent on temperature and grain size. According to [50], in the case of varying parameter a_1 the 6th-order potential is structurally stable, and in the case of varying parameters a_1 and a_2 , the 10th-order potential is stable. Although (21) and (22) with one varying parameter are stable, when varying several external

parameters, such as temperature and grain size, the phase transitions cannot be sufficiently explained by them. The first-principles investigation showed that the coefficients of the quadratic and two fourth power terms in the Landau potential for BaTiO₃ are all strongly temperature dependent [61]. Also, according to the results of singularity theory [47, 50] and the calculation of the coefficient phase diagram [50], the phase diagram including the triple points C–T–O and C–O–R and the C–O phase transition lines observed experimentally in BT nanoceramics is obtained based on the structurally-stable thermodynamic potential model (7) with the three parameters a_1 , a_2 , and a_{11} varying with the external thermodynamical variables. However, in the previous phenomenological theories, the parameters a_1 or a_1 and a_2 in the potential model (21) or (22) were chosen as the varying parameters, and the structural stability of the potential was not taken into account. Hence, the phase transition characteristics observed in BaTiO₃ nanoceramics have not been accurately explained. Thus, the qualitative features of the experimental temperature–grain size phase diagram, the existence of two triple points (C–T–O and C–O–R), and the O–C phase line could not be explained by the previous phenomenological theories.

Considering the experimental measurements [14, 19–25], the results of the singularity theory [47, 50], and the calculation results for the coefficient phase diagrams of the potentials [50], we have chosen the 8th-order LGD potential (7) with the varying parameters, a_1 , a_2 , and a_{11} . All the varying parameters have been assumed as a function of temperature and grain size — see (8). The phase diagram based on the LGD potential (7) explains well the experimental data on the decrease in the C–T phase transition points and the increase in T–O and O–R ones with decreasing grain size and reproduces correctly the triple points (C–T–O and C–O–R) and the ferroelectric reentrance phenomenon. We have calculated the temperature and grain size dependences of the polarization and dielectric properties of BaTiO₃ nanoceramics on the basis of the LGD potential (7). The jumps in spontaneous polarization are shown at the phase transition temperatures (Fig. 3). The jump values decrease with decreasing grain size. With decreasing grain size, the polarizations decrease in the T and O phases, whereas in the R phase, they increase. The temperature dependence of the dielectric constant at various grain sizes exhibits decreasing dielectric jumps and diffusing peaks when decreasing grain size. The dielectric constant increases with increasing grain size, and the dielectric anomalies appear at the grain sizes of 14, 23, and 67 nm at room temperature. Our calculated results are in good agreement with the experimental ones for dielectric anomalies at the phase transition temperatures. However, our calculated results above about 100 nm show a slower increase than the experimental ones, which

can be attributed to the assumption of the single domain state in the grains and to the consideration of the boundary layer effect.

6. Conclusions

In the present paper, the LGD theory based on the structurally stable thermodynamic potential with 3 varying parameters has been proposed for BaTiO₃ nanoceramics. The varying parameters, the 2nd- and 4th-order coefficients, have been assumed to be dependent on temperature and grain size. The characteristics of the theoretical temperature–grain size phase diagram agree with the experimental data for the C–T–O and C–O–R triple points and ferroelectric to paraelectric to ferroelectric reentrance phenomenon. The calculation results on the polarization and dielectric properties of the BaTiO₃ nanoceramics explain well the size effect observed in experiments. An increase in the spontaneous polarization in the R phase supports the ferroelectric reentrance phenomenon.

Appendix

Let χ_{ij} be the components of the dielectric susceptibility tensor in the pseudo-cubic coordinate system. They are diagonalized in the new coordinate system

$$\begin{pmatrix} \chi_{11} & \chi_{12} & \chi_{13} \\ \chi_{21} & \chi_{22} & \chi_{23} \\ \chi_{31} & \chi_{32} & \chi_{33} \end{pmatrix} \Rightarrow \begin{pmatrix} \chi'_{11} & & \\ & \chi'_{22} & \\ & & \chi'_{33} \end{pmatrix}, \quad (23)$$

where χ_{ij} is obtained from

$$\chi_{ij}^{-1} = \eta_{ij} = \frac{\partial^2 \Phi}{\partial p_i \partial p_j}. \quad (24)$$

The inverse dielectric susceptibilities for each lower symmetry phase are obtained as follows:

• T phase

The η_{ijT} in the T phase in the pseudo-cubic system are as follows

$$\begin{aligned} \eta_{11T} = \eta_{22T} &= 2a_1 + 2(2a_{11} + a_2) p_t^2 \\ &+ 2(3a_{111} + a_{12}) p_t^4 + 2(4a_{1111} + a_{112}) p_t^6, \\ \eta_{33T} &= 2a_1 + 12a_{11} p_t^2 + 30a_{111} p_t^4 + 56a_{1111} p_t^6. \end{aligned} \quad (25)$$

The spontaneous polarization in the T phase is oriented along the [001] direction of the original cubic unit cell, so that the average dielectric constant (see (19)) in the new coordinate system is obtained as follows

$$\varepsilon_g = \frac{1}{3\varepsilon_0} \left(\frac{2}{\eta_{11T}} + \frac{1}{\eta_{33T}} \right) + 1. \quad (26)$$

• O phase

$$\begin{aligned} \eta_{11O} = \eta_{33O} &= 2a_1 + 2(8a_{11} + a_2) p_o^2 \\ &+ 2(36a_{111} + 7a_{12}) p_o^4 + 4(64a_{1111} + 3a_{22} + 14a_{112}) p_o^6, \\ \eta_{22O} &= 2a_1 + 4(a_{11} + a_2) p_o^2 + 2(12a_{111} + 5a_{12} + a_3) p_o^4 \\ &+ 4(16a_{1111} + 2a_{22} + 6a_{112}) p_o^6, \\ \eta_{31O} = \eta_{13O} &= 4(2a_{11} + a_2) p_o^2 + 16(3a_{111} + a_{12}) p_o^4 \\ &+ 4(48a_{1111} + 4a_{22} + 14a_{112}) p_o^6, \\ \eta_{12O} = \eta_{21O} = \eta_{23O} = \eta_{32O} &= 0. \end{aligned} \quad (27)$$

The spontaneous polarization is oriented along the [101] direction of the cubic unit cell, and the transformation matrix from the old coordinate system to the new one is written as follows

$$\mathbb{A}_O = \begin{pmatrix} a' \\ b' \\ c' \end{pmatrix} = \begin{pmatrix} \frac{1}{\sqrt{2}} & 0 & \frac{-1}{\sqrt{2}} \\ 0 & 1 & 0 \\ \frac{1}{\sqrt{2}} & 0 & \frac{1}{\sqrt{2}} \end{pmatrix} \begin{pmatrix} a \\ b \\ c \end{pmatrix}. \quad (28)$$

Using the 2nd rank tensor transformation, the dielectric constant is written as follows

$$\varepsilon_g = \frac{1}{3\varepsilon_0} \left[\frac{1}{(\eta_{11O} - \eta_{13O})} + \frac{1}{\eta_{22O}} + \frac{1}{(\eta_{11O} + \eta_{13O})} \right] + 1. \quad (29)$$

• R phase

$$\begin{aligned} \eta_{11R} = \eta_{22R} = \eta_{33R} &= 2a_1 + 4(5a_{11} + a_2) p_r^2 \\ &+ 2(63a_{111} + 17a_{12} + a_3) p_r^4 + 8(81a_{1111} + 7a_{22} \\ &+ 24a_{112}) p_r^6, \\ \eta_{12R} = \eta_{13R} = \eta_{21R} = \eta_{23R} = \eta_{31R} = \eta_{32R} &= \\ &4(2a_{11} + a_2) p_r^2 + 4(18a_{111} + 7a_{12} + a_3) p_r^4 \\ &+ 4(108a_{1111} + 14a_{22} + 39a_{112}) p_r^6. \end{aligned} \quad (30)$$

The spontaneous polarization of the R phase is oriented along the body diagonal of the cubic unit cell. Considering the transformation of the coordinate system

$$\mathbb{A}_R = \begin{pmatrix} a' \\ b' \\ c' \end{pmatrix} = \begin{pmatrix} \frac{1}{\sqrt{2}} & -\frac{1}{\sqrt{2}} & 0 \\ \frac{1}{\sqrt{6}} & \frac{1}{\sqrt{6}} & -\frac{2}{\sqrt{6}} \\ \frac{1}{\sqrt{3}} & \frac{1}{\sqrt{3}} & \frac{1}{\sqrt{3}} \end{pmatrix} \begin{pmatrix} a \\ b \\ c \end{pmatrix}, \quad (31)$$

the average dielectric constant is written as follows

$$\varepsilon_g = \frac{1}{3\varepsilon_0} \left[\frac{2}{(\eta_{11R} - \eta_{12R})} + \frac{1}{(\eta_{11R} + 2\eta_{12R})} \right] + 1. \quad (32)$$

Acknowledgments

The authors are indebted to the anonymous reviewers and editor, whose valuable criticisms and suggestions during revision helped to correct some errors in the original manuscript.

References

- [1] Y. Feng, J.L. Li, W.L. Li, M.L. Li, Q.G. Chi, T.D. Zhang, W.D. Fei, *Compos. Part A Appl. Sci. Manuf.* **125**, 105524 (2019).
- [2] B.S. Ahmed, M.B. Nandaprakash, K. Namratha, K. Byrappa, R. Somashekar, *Phys. Status Solidi B* **2018**, 1700581 (2018).
- [3] J.J. Wang, E.A. Eliseev, X.Q. Ma, P.P. Wu, A.N. Morozovska, L.-Q. Chen, *Acta Mater.* **59**, 7189 (2011).
- [4] D. Machon, L. Piot, D. Hapiuk et al., *Nano Lett.* **14**, 269 (2014).
- [5] T. Bolstad, K. Kjærnes, K. Raa, R. Takahashi, M. Lippmaa, T. Tybell, *Mater. Res. Express* **6**, 056409 (2019).
- [6] Y.Q. Tan, J.L. Zhang, Y.Q. Wu et al., *Sci. Rep.* **5**, 9953 (2015).
- [7] C. Chen, H. Hao, T. Wang, J.S. Cheng, Z.P. Luo, L. Zhang, M.H. Cao, Z.H. Yao, H.X. Liu, *Ceram. Int.* **45**, 7166 (2019).
- [8] M.A. Gomes, L.G. Magalhães, A.R. Paschoal, Z.S. Macedo, Á.S. Lima, K.I.B. Eguiluz, G.R. Salazar-Banda, *J. Nanomater.* **2018**, 5167182 (2018).
- [9] Z. Zhao, V. Buscaglia, M. Viviani, M.T. Buscaglia, L. Mitoseriu, A. Testino, M. Nygren, M. Johnsson, P. Nanni, *Phys. Rev. B* **70**, 024107 (2004).
- [10] V. Buscaglia, M. Viviani, M.T. Buscaglia et al., *Powder Technol.* **1148**, 24 (2004).
- [11] C. Pithan, Y. Shiratori, R. Waserz, J. Dornseiffer, F.-H. Haegel, *J. Am. Ceram. Soc.* **89**, 2908 (2006).
- [12] X.Y. Deng, X.H. Wang, H. Wen, L.L. Chen, L. Chen, L.T. Li, *Appl. Phys. Lett.* **88**, 252905 (2006).
- [13] M.T. Buscaglia, M. Viviani, V. Buscaglia et al., *Phys. Rev. B* **73**, 064114 (2006).
- [14] M.H. Frey, D.A. Payne, *Phys. Rev. B* **54**, 3158 (1996).
- [15] G. Arlt, D. Hennings, G. de With, *J. Appl. Phys.* **58**, 1619 (1985).
- [16] B.R. Li, X.H. Wang, L.T. Li, H. Zhou, X.T. Liu, X.Q. Han, Y.C. Zhang, X.W. Qi, X.Y. Deng, *Mater. Chem. Phys.* **83**, 23 (2004).
- [17] X.Y. Deng, X.H. Wang, H. Wen, A.G. Kang, Z.L. Gui, L.G. Li, *J. Am. Ceram. Soc.* **89**, 1059 (2006).
- [18] V. Buscaglia, M.T. Buscaglia, M. Viviani et al., *J. Eur. Ceram. Soc.* **25**, 3059 (2005).
- [19] A.V. Polotai, A.V. Ragulya, C.A. Randall, *Ferroelectrics* **288**, 93 (2003).
- [20] D. McCauley, R.E. Newnham, C.A. Randall, *J. Am. Ceram. Soc.* **81**, 979 (1998).
- [21] C.A. Randall, *J. Ceram. Soc. Jpn.* **109**, S2 (2001).
- [22] M.H. Frey, Z. Xu, P. Han, D.A. Payne, *Ferroelectrics* **206**, 337 (1998).
- [23] M. Tanaka, Y. Makino, *Ferroelectrics Lett.* **24**, 13 (1998).
- [24] Y. Fukui, S. Izumisawa, T. Atake, A. Hamano, T. Shirakami, H. Ikawa, *Ferroelectrics* **203**, 227 (1997).
- [25] J.L. Zhu, S. Lin, S.M. Feng, L.J. Wang, Q.Q. Liu, *J. Appl. Phys.* **112**, 124107 (2012).
- [26] Y.L. Li, Z.Y. Liao, F. Fang, X.H. Wang, L.T. Li, J. Zhu, *Appl. Phys. Lett.* **105**, 182901 (2014).
- [27] L.D. Landau, E.M. Lifshitz, *Statistical Physics*, Pergamon Press, Oxford 1980.
- [28] P. Lv, L.H. Wang, C.S. Lynch, *Acta Mater.* **137**, 93 (2017).
- [29] W.R. Buessem, L.E. Cross, A.K. Goswami, *J. Am. Ceram. Soc.* **49**, 33 (1966).
- [30] D. Ricinshi, V. Tura, L. Mitoseriu, M. Okuyama, *J. Phys. Condens. Matter* **11**, 1601 (1999).
- [31] C. Fang, D.X. Zhou, S.P. Gong, W. Luo, *Phys. Status Solidi B* **247**, 219 (2010).
- [32] C. Fang, L.Y. Chen, D.X. Zhou, *Physica B* **409**, 83 (2013).
- [33] C. Fang, D.X. Zhou, S.P. Gong, *Physica B* **406**, 1317 (2011).
- [34] Y.L. Li, L.E. Cross, L.Q. Chen, *J. Appl. Phys.* **98**, 064101 (2005).
- [35] S. Lin, T.Q. Lü, C.Q. Jin, X.H. Wang, *Phys. Rev. B* **74**, 134115 (2006).
- [36] T.Y. Sun, X.H. Wang, H. Wang, X.Q. Zhang, Z.D. Cheng, C.Q. Sun, L.T. Li, *J. Am. Ceram. Soc.* **93**, 2571 (2010).
- [37] J.H. Qiu, Q. Jiang, *J. Appl. Phys.* **105**, 034110 (2009).
- [38] V.I. Arnold, *Catastrophe Theory*, 3rd ed. Springer Verlag, Berlin 1992.
- [39] D.P.L. Castringiano, S.A. Hayes, *Catastrophe Theory*, Taylor & Francis Group, CRC press, 2018.
- [40] A.M. Prohorov, Y.M. Gufan, E.S. Larin, E.G. Rudashevski, V.B. Shirokov, *Sov. Phys. Dokl.* **29**, 656 (1984).
- [41] E.I. Kut'in, V.L. Lorman, S.V. Pavlov, *Sov. Phys. Usp.* **34**, 497 (1991).
- [42] P. Toledano, V. Dmitriev, *Reconstructive Phase Transitions in Crystals and Quasicrystals*, World Scientific, Singapore 1996.

- [43] I.A. Sergienko, Y.M. Gufan, S. Urazhdin, *Phys. Rev. B* **65**, 144104 (2002).
- [44] G. Gaeta, *Ann. Phys.* **312**, 511 (2004).
- [45] G. Gaeta, *J. Math. Phys.* **56**, 083504 (2015).
- [46] L. Li, I.-H. Kim, K.-O. Jang, K.-S. Ri, J.-C. Cha, *J. Appl. Phys.* **114**, 034104 (2013).
- [47] I.-H. Kim, K.-O. Jang, I.-H. Kim, P.-S. O, S.-N. Ju, *Physica B* **690**, 416157 (2024).
- [48] S.V. Pavlov, *Moscow Univ. Phys. Bull.* **71**, 508 (2016).
- [49] V.M. Talanov, V.B. Shirokov, M.V. Talanov, *Acta Cryst. A* **71**, 301 (2015).
- [50] I.-H. Kim, K.-O. Jang, I.-H. Kim, L. Li, *Phase Transit.* **91**, 239 (2018).
- [51] I.-H. Kim, I.-H. Kim, K.-O. Jang, K.-R. Sin, C.-J. Kim, *Phase Transit.* **91**, 1189 (2018).
- [52] I.-H. Kim, I.-H. Kim, S.-G. Im, K.-O. Jang, *Physica B* **639**, 413961 (2022).
- [53] K.-O. Jang, I.-H. Kim, I.-H. Kim, S.-G. Im, K.-R. Sin, C.-J. Kim, *Phase Transit.* **93**, 439 (2020).
- [54] P. Tolédano, *EPJ Web Conf.* **22**, 00007 (2012).
- [55] K. Uchino, E. Sadanaga, T. Hirose, *J. Am. Ceram. Soc.* **72**, 1555 (1989).
- [56] W. Martienssen, H. Warlimont, *Springer Handbook of Condensed Matter and Materials Data*, Springer, Berlin 2005.
- [57] I.N. Leontyev, O.E. Fesenko, N.G. Leontyev, B. Dkhil, *Appl. Phys. Lett.* **96**, 142904 (2010).
- [58] T. Yamada, *J. Appl. Phys.* **43**, 328 (1972).
- [59] A.Y. Emelyanov, N.A. Pertsev, S. Hoffmann-Eifert, U. Bottger, R. Waser, *J. Electroceram.* **9**, 5 (2002).
- [60] X. H. Wang, H. Wen, R. Z. Chen, H. Zhou, L. T. Li, in: *IEEE Int. Ultrasonics, Ferroelectrics, and Frequency Control Joint 50th Anniversary Conf., Montréal, Canada*, 2004, p. 324.
- [61] A.I. Sokolov, *Phys. Solid State* **51**, 351 (2009).